8-2014

Aluminum Monoxide Emission Measurements Following Laser-Induced Breakdown for Plasma Characterization

David Michael Surmick
University of Tennessee - Knoxville, dsurmick@utk.edu

To the Graduate Council:

I am submitting herewith a thesis written by David Michael Surmick entitled "Aluminum Monoxide Emission Measurements Following Laser-Induced Breakdown for Plasma Characterization." I have examined the final electronic copy of this thesis for form and content and recommend that it be accepted in partial fulfillment of the requirements for the degree of Master of Science, with a major in Physics.

Christian G. Parigger, Major Professor

We have read this thesis and recommend its acceptance:

Horace Crater, Joseph Majdalani

Accepted for the Council:
Carolyn R. Hodges

Vice Provost and Dean of the Graduate School

(Original signatures are on file with official student records.)

Aluminum Monoxide Emission Measurements Following Laser-Induced Breakdown for Plasma Characterization

A Thesis Presented for the
Master of Science
Degree
The University of Tennessee, Knoxville

David Michael Surmick
August 2014

Dedication

This work is dedicated to my parents, John A. and Cathy J. Surmick,
for their never ending support, encouragement, and dedication to their children.

Acknowledgements

This work would not have been able to be completed without the help of others. I would like to recognize the following people and organizations for their support of this work and aid in completing it:

Dr. Christian Parigger
Dr. Horace Crater
Dr. Joseph Majdalani
The University of Tennessee
The University of Tennessee Space Institute
The Center for Laser Applications
James Hornkohl
Alexander Woods
Michael Witte
Lauren Swafford

Abstract

In this work, spectroscopic emissions from laser ablated aluminum samples are used to characterize the time dependent decay of laser-induced plasma. The plasma is created by tightly focusing nanosecond pulsed laser radiation. Time resolved measurements of the plasma are made with a gated, intensified linear diode array coupled to an optical multichannel analyzer and/or an intensified charged coupled device. Time resolution is achieved by synchronizing the laser with the measurement rate of the array detector.

Computed diatomic molecular aluminum monoxide emissions were used to infer the temperature of the plasma as a function of time. This was completed by comparing experimentally collected spectra to theoretical calculations with a Nelder-Mead algorithm. The theoretical spectra were calculated from accurate line strengths for selected aluminum monoxide bands. The temperature of the plasma was found to decrease from typically 5100 Kelvin to 3600 Kelvin from 10 to 90 microseconds after optical breakdown. The temperature appears to plateau to a temperature of 3800 Kelvin after 90 microseconds. Error analysis in the inferred temperature is accomplished with the fitting algorithm and the precision was found to be between 45 and 75 Kelvin. Gated camera measurements were performed to infer the temperature along the height of the plasma and found the temperature profile of the plasma to increase above the plasma edge. Superposition of hydrogen Balmer series beta emissions with aluminum monoxide spectra allow one to infer electron number densities from the plasma at time delays preceding 20 microseconds.

Table of Contents

List of Tables

List of Figures

Chapter 1

Introduction and General Information

Lasers are some of the most practical and useful inventions of the twentieth century as they have developed into useful experimental tools in applied research. One of the applications of laser radiation is in the field of spectroscopy, particularly with the use of pulsed laser radiation to induce optical breakdown in gas or near the surface of a target sample. This is known as laser-induced optical breakdown and each laser pulse produces a micro-sized, laboratory scale plasma. This is achieved by tightly focusing the laser radiation so that the breakdown threshold, the characteristic amount of irradiance required to induce breakdown for a given material, is reached at a given set of experimental conditions. The breakdown threshold of a material is measured in terms of the irradiance, which is the power per area delivered to a sample. Pulsed laser radiation is advantageous for this application, as compared to continuous wave laser radiation, and typically a nanosecond or femtosecond pulsed laser is used. The peak power delivered to the surface of the sample from a pulsed laser is greater than that of a continuous wave laser since the energy of the pulsed laser is delivered over a much shorter time duration. The typical focused spot size is on the order of 50-100 microns and as such, the energy per pulse of the laser determines the irradiance incident on a sample. With conditions similar to the ones described it is possible to achieve an irradiance between 1-10,000 GW/cm^2 at atmospheric pressure for a sample.(1)

Once the plasma is created one may observe it through its unique spectroscopic emissions. This is known as laser-induced breakdown spectroscopy (LIBS) and the spectroscopic signal can be manipulated in many ways to characterize the laser-induced plasma.(2-4) LIBS has industrial applications in determining the composition of materials, (5-7) and this principle has been expanded to include applications in geophysics and planetary science, as the Mars rover Curiosity has been outfitted with a LIBS apparatus.(8) One of the advantages of LIBS in research applications is ability to be used in time resolved studies. This allows for characterization of the time evolution of laser-induced plasma through a number of parameters such as the temperature and electron number density. This has been extensively investigated for solids, liquids, and gases. In this study, the temporal evolution of laser-induced plasma on the surface of an aluminum target is studied through spectroscopic emission of atomic lines and diatomic molecular aluminum monoxide (AlO) spectra.

Plasma Radiation Processes

All plasmas emit or absorb radiation either in the form of discrete or continuous emissions. Examples of continuum emissions are thermal radiation and radiation from recombination. Plasmas are thermal radiators and as such emit continuum radiation according to Planck's law. Recombination occurs as free electrons recombine with ions in the plasma. An example of discrete emissions are the radiation of electrons undergoing transitions between the energy levels in atoms, ions, and molecules, which produce corresponding atomic and molecular spectra. In terms of the decay of plasma,

recombination dominates the plasma emission at early times up to 100 to 200 nanoseconds following the formation the plasma.(9) After the plasma has cooled sufficiently ions and atoms will be able to form and will emit line radiation. This typically begins to occur after hundreds of nanoseconds following initiation of the laser-induced plasma. Early in the plasma decay, atomic emission lines will be much broader due to several processes occurring within the plasma, such as influences from external magnetic and electric fields which cause Stark broadening and collisions.(10, p365) Molecules also form in plasma, however this occurs much later in the plasma decay since molecules are, in general, stable for significantly lower temperature than atoms and ions, and will typically begin to form after tens of microseconds following plasma formation.

There are two forms of line radiation, spontaneous and induced. In general plasmas experience spontaneous emission unless there is an interaction with an external field, such as a laser. Spontaneous emissions occur as electrons naturally transition between an upper state and a lower state.(11, p87) The rate at which this occurs is related to a quantity known as the transition probability, also named the Einstein A coefficient, and is characteristic to a specific transition. As such, the emission of photons for an energy transition is related to the density of electrons undergoing a specific transition. This information may be obtained from the spectral radiance of an atomic line which is described by a quantity known as the emission coefficient or local emission coefficient. This quantity is defined as the radiant flux in the plasma from a given volume element emitting through specific solid angle.(11, p6) The local emission coefficient may be

obtained by de-convolving emission spectra.(12,13) The de-convolution is required since a spectral measurement is the convolution of the actual measurement and the instrument function, the broadening of a line due to the extent of the spectrometer slit, and will also give depth information on the plasma.

Molecular transitions in the visible and ultraviolet wavelength regions correspond, for the most part, with electronic transitions. Electronic transitions, or electronic spectra, occur for molecular spectra in which there are transitions for the electronic energy level as well as possible rotational and vibrational states.(14, p549) Rotational and vibrational states exist due to the added degrees of freedom of the multi-atomic system. The spectra of molecules are tightly packed with lines from both vibrational and rotational transitions. Due to the tight packing of these lines, molecular emissions take on the appearance of bands. Each band is characterized by a change in vibrational state and the accompanying rotational state changes. Figure 1 is a theoretical calculation of the spectra of the diatomic molecule aluminum monoxide for the $\Delta v=0$ band, meaning no changes in vibrational state in the diatomic potential well, displaying both vibrational and rotational structure. The spectra are calculated with a resolution of 0.09 nm and an emission temperature of 4000 Kelvin with a normalized intensity emission of 1000 arbitrary units.

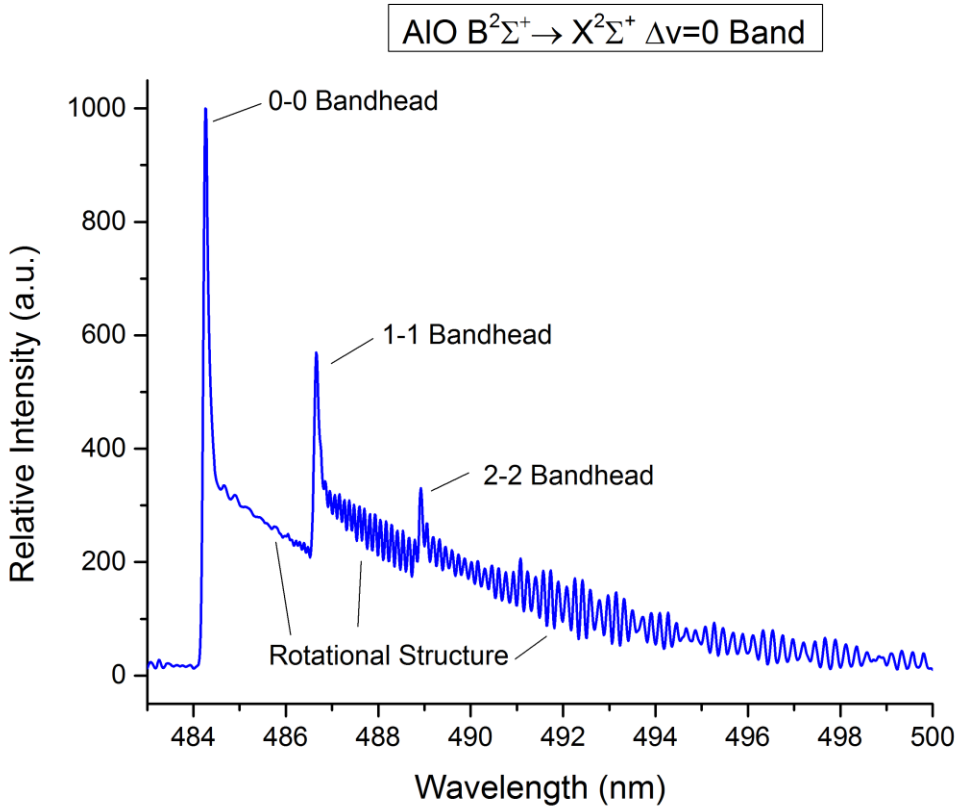

Figure 1. Theoretical calculation of AlO Δv=0 spectrum. Highlighted are the 0-0, 1-1, and 2-2 vibrational peaks as well as the accompanying rotational structure.

Line Broadening

This study will use the broadening of atomic emissions to characterize laser-induced plasma. Prior to discussing how atomic and molecular emission lines are broadened in plasma, it is helpful to briefly discuss how the shape of the lines are represented. For the purposes of this study only the broadening of atomic emission lines are considered, however both atomic and molecular spectra are broadened. The line shape or line profile, *L(λ)*, is the mathematical representation of an atomic or molecular emission and is a function of the wavelength or frequency. The line shape is defined by two important parameters, the center wavelength, λ_0, and the full width at half maximum (FWHM), $\lambda_{1/2}$, of the line. Two of the most common functions used to describe the shape of a line are the Gaussian and Lorentzian functions (11, p153)

$$L_G(\lambda) = \sqrt{\frac{4\ln(2)}{\pi}}\frac{1}{\lambda_{1/2}}\exp\left(-4\ln(2)\left(\frac{\lambda-\lambda_0}{\lambda_{1/2}}\right)^2\right) \quad (1)$$

$$L_L(\lambda) = \frac{1}{2\pi}\frac{\lambda_{1/2}}{(\lambda-\lambda_0)^2+\frac{\lambda_{1/2}^2}{4}} \quad (2)$$

which are normalized and given as a function of the wavelength position.

A third line profile that is commonly considered is the Voigt profile which is a convolution of the Gaussian and Lorentzian functions. The result of using the Voigt profile is that Gaussian and Lorentzian line shape characteristics may be considered simultaneously when describing a line shape. The Voigt profile is given by

$$L_v(\lambda) = \sqrt{\frac{4\ \ln(2)}{\pi}}\ \frac{a}{\pi\lambda_{1/2}^{G}} \int_{-\infty}^{\infty} \frac{e^{-t^2}dt}{a^2+(x-t)^2} \tag{3}$$

where $\lambda_{1/2}^{G}$ is the Gaussian half width, a is the parameter that defines the weights of the Gaussian and Lorentzian contributions, and x represents the wavelength parameter. The wavelength parameter, x, is given by

$$x = 2\sqrt{\ln(2)}\ \frac{\lambda-\lambda_0}{\lambda_{1/2}^{G}} \tag{4}$$

and the Voigt parameter, a, is given by

$$a = \sqrt{\ln(2)}\ \frac{\lambda_{1/2}^{L}}{\lambda_{1/2}^{G}}\ , \tag{5}$$

where $\lambda_{1/2}^{L}$ is the Lorentzian half width.(6,p153-154) In the Voigt profile, Gaussian characteristics dominate the central region of the line shape while Lorentzian characteristics are dominant in the wings, or edges. Regardless of the type of profile used to describe an emission line, the physical interpretation of the line shape is the distribution of electrons undergoing the associated atomic transition of a particular emission line.

Line broadening in plasma occurs due to a number of different effects such as Doppler and Stark effects. Doppler broadening is the result of shifts in the frequency of an emission line due to motion of the emission source within the plasma and Stark broadening occurs as the result of pressure broadening due to the presence of electrons and ions in plasma. In terms of decaying plasma, Stark broadening tends to be the most

dominant, especially early in the decay of the plasma due to the increased number of electrons and ions present. By studying Stark broadened lines, it is possible to infer two important parameters that define the decay of plasma, the electron number density, N_e and electron excitation temperature, T_e.(15-17)

Applications of Laser-Induced Plasma

The methods of laser-induced breakdown have spectroscopy evolved into an ideal on-site experimental tool due to its low costs, portability, relative experimental ease, and ability to be used with solid, liquid and gaseous samples. Many applications of LIBS take advantage of the unique spectroscopic signal from laser-induced plasma to identify the elemental composition of a sample of interest. This analysis is popular in geological (18) and forensic applications (19) where the parameter of interest is the integrated area of a collected broadband spectrum. Spectra, both atomic and molecular in nature, may be used to determine characteristic plasma parameters and conditions. One of the most heavily studied atomic spectra from a laser-induced breakdown event is that of hydrogen. Hydrogen atomic lines are broadened when observed from hot plasma due to the strength of the linear Stark effect in the hydrogen atom. This effect may be taken advantage of to determine the electron number density, N_e, of a plasma through relations between the N_e and broadened line width. Relationships between the N_e of Stark broadened line widths are primarily empirical in nature and are determined through direct experimentation of LIBS in hydrogen environments. Experiments with observations of hydrogen Balmer

series emissions have been performed from breakdown events initiated in both pure hydrogen gas and laboratory air environments.

In a recent study of line shape profiles and broadening mechanisms in atomic hydrogen spectra by N. Konjević *et al.* (20), empirical formulae were determined for the hydrogen Balmer series H_α, H_β, and H_γ lines as a function of the Stark width from experimental hydrogen spectra. The best line profile functions for determining the Stark broadening parameter were found through deconvolution of the atomic spectra and it was determined that a Lorentzian line profile best minimizes the error in the Stark line width. Fitting to determined line widths found the following relationship for H_β N_e in units of m^{-3} as a function of the Stark width, w_s,

$$N_e = 10^{22} \times \left(\frac{w_s}{0.94666}\right)^{1.49} \tag{6}$$

where w_s is determined in units of nm. It should be noted that this empirical formulation is only valid for the region for N_e of 1.5 to 30×10^{24} m^{-3}.

In a different study by Parigger *et al.* (15), N_e values were determined from measurements of H_α and H_β from a pure hydrogen environment that was slightly above atmospheric pressure to determine the number density in the range of 10^{22} to 10^{24} m^{-3}. Rather than use the conventional theory of Griem (21,22), the convergent theory of Oks (23,24), which has been tested against benchmark experiments and includes more physical phenomena than the theory of Griem, was used to determine N_e as high as 10^{25} m^{-3} from H_β emissions which were in agreement with inferred N_e from H_α measurements

at times less than 1 μs following optical breakdown. Further, in a recent study of H_α and H_β emissions from a laser-induced plasma, a comparison was made between the theories of Oks and Konjević. It was determined that Oks convergent theory is preferred for plasmas that have lower number densities.(25) It should be noted that the best accuracy that is achievable for inferences of the N_e from H_β emissions are within ten percent of the actual value as compared to almost twenty percent for H_α emissions.

Molecular spectra collected from a laser-induced breakdown event may also be used to characterize the conditions of plasma. Diatomic molecular spectra that have been used to characterize laser-induced plasma include AlO, CN, C_2, and TiO (26-29) for various applications including support of combustion diagnostics and micromachining applications. Of particular interest to this study are the emissions of aluminum containing molecules from laser-induced plasma. In industrial applications laser ablation of aluminum has been used to determine the purity of aluminum alloys through temperature characterizations of the plasma with Boltzmann plotting methods. This method infers the temperature by fitting the intensity of several spectral lines, considered with atomic constants such as the transition probability and degeneracy factor, against the upper energy level.(30) The slope of the plot is then used to infer the temperature from the Boltzmann equation. The broadening of aluminum atomic lines has also been used to infer N_e values for the purposes of identifying the difference between molten and solid aluminum alloys.(31) Studies have also been coupled with time resolution to infer plasma characteristics as function of time. This was performed in a study in which an aluminum

rod in the presence of different bath gases was laser ablated.(32) Boltzmann plotting methods were used with the intensity ratios of aluminum atomic line emissions at 308, 309, 394, and 396 nm to infer the plasma temperature as a function of time. Temperatures were found to be on the order of 4000 Kelvin for breakdown in air.

In addition to using atomic lines to infer plasma temperature, diatomic molecular emissions may also be considered for this application. Aluminum monoxide is an early, intermediate product in the oxidation of aluminum and its emissions were utilized to determine temperatures in the laser ablation of an aluminum sheet in a spatial and temporal study of aluminum micro-plasma.(33) Temperatures were reported to be 4250 Kelvin for a time of 50 μs following breakdown. In another study to investigate the use of aluminum laser-induced plasma in micromachining applications, AlO spectra were used to probe the temperature of laser-induced plasma.(34,35) The inferred temperatures were found to be approximately 4000 Kelvin at a time of 50 μs following breakdown. The experiments in references (34) and (35) were performed in the presence of a hydrogen atmosphere and as such hydrogen atomic emissions were also observed. Coupled with observed aluminum atomic line emissions, N_e values of 10^{23} m^{-3} at a time of 1 μs following breakdown. Recent results of laser-ablation of an aluminum sample have shown temperatures to be 4880 ± 95 Kelvin at 45 μs and 4420 ± 80 Kelvin at 70 μs following breakdown near the surface of an aluminum sample.(36) The temperature results of the previously completed aluminum laser ablation studies discussed are summarized in Table 1 at the end of this chapter. In this study, the emission of laser-

induced plasma near the surface of an aluminum alloy target is characterized from its spectroscopic emissions from time resolved LIBS measurements. The plasma is generated by tightly focusing 1064 nm Nd:YAG nanosecond pulsed laser radiation on the surface of an aluminum sample. Following breakdown, diatomic molecular AlO spectral measurements are made with a gated, intensified linear diode array to infer the temporal temperature decay of the plasma. Measurements with an intensified charged couple device are also used to infer the temperature behavior along the height of the vertical axis of the plasma. Further, measurements of atomic H_β with AlO spectra collected with the linear diode array are used to infer the electron number density at early observed times following breakdown.

Table 1. Summary of the temperature results from previously completed aluminum LIBS studies.

Reference Number	**Temperature (Kelvin)**	**Time Delay (μs)**	**Temperature Inference Method**
32	4000	20	Al Boltzmann Plot
33	4250	50	Al Boltzmann Plot
34 and 35	4000	50	AlO Fitting
36	4880	45	AlO Fitting

Chapter 2

Experimental Methods

The goal of this study is to characterize the temporal decay of laser-induced plasma generated near the surface of an aluminum target. This was accomplished using time resolved LIBS. Laser light from a nanosecond pulsed Nd:YAG Q-switched (Quanta Ray) laser operating in its fundamental mode with 1064 nm radiation and a pulse width of 12 ns was used to ablate an aluminum target. The target was an aluminum plate made of aluminum alloy 6061. The laser radiation was focused such that the laser was incident vertically downward on the target. This orientation was achieved with the use of three 50/50 beam splitters. The laser light was focused to a spot size of approximately 50 microns with 10.0 cm focal length lens. The orientation of the laser was chosen to create axially symmetric vertical plasma such that line of sight measurements could be made. The typical energy per pulse of the laser at the point of breakdown was 190 mJ with a corresponding irradiance of approximately 2 GW/cm^2.

Following laser-induced breakdown on the aluminum target, line of sight spectral measurements were made from the plasma and plasma plume. Light from the plasma was focused onto the entrance slit of Jobin-Yvon HR640 scanning spectrometer with f/5.2 optics, matched to the f-number of the spectrometer to optimize light throughput and grating performance. The spectrometer is a Czerny-Turner style spectrograph and was operated with an 1800 grooves/mm grating. The entrance slit of the spectrometer was reduced to the smallest possible extent to reduce the instrument function as much as

possible and was open to a size of approximately 100 microns. After the light is dispersed by the spectrometer, it is focused onto the chip of a detector. The detectors for this study were a gated, intensified linear diode array (EG and G PARC 1421 UV) coupled with an optical multichannel analyzer (OMA) (Princeton Instruments 1460) and an intensified charged coupled device (ICCD) (model Andor iStar DH 34T-250-03). The linear diode array is a horizontal array of 1024 pixels while the ICCD is a rectangular detector with 1024 vertical pixels and 1024 horizontal pixels. The vertical pixels of the ICCD may be binned together to increase data processing speeds and maximize the measured spectral signal while still recording spatially resolved data along the height of the entrance slit and, hence, the height of the plasma. In order to reduce the effects of variations from laser shot to laser shot, each of the spectra collected in this study is the accumulation of 100 breakdown events.

Each measurement was made at a specific time following the formation of the plasma. Additionally, the amount of time the detector was exposed to the dispersed light from the spectrometer was controlled. These two quantities are called the time delay and gate width, respectively. In practice, the goal of the time synchronization is to link the data acquisition with the timing of the laser pulse. For experiments involving the OMA, differences in the laser repetition rate and the data acquisition speed needed to be considered. The laser repetition rate is 10 Hz. while the OMA operates at 50 Hz. The exact timing of the delay and gate is achieved with the use of waveform and delay generators. The waveform generator (Wavetek FG36 function generator) and pulse

generator (Stanford Research Systems model DG535) are used synchronously to externally trigger the linear diode array and OMA. The waveform generator is operated at 50 Hz. with a triangular pulse that is converted to a 10 Hz. signal with a custom built divide by five synch box which acts as a relay with the waveform generator to create an accurate zero point from which the time resolution is measured. The outputs of the synch box are connected both to the laser and a delay generator (Berkley Nucleonics Corp. 6040 universal pulse generator) which controls when the trigger pulse is sent to the OMA/linear diode array. This communicates at what delay to make the measurement and how long the detector is exposed. The delay generator controls both the gate and delay. Figure 2 shows a layout of the timing apparatus used to achieve time resolution with the linear diode array experiments. A detailed description of the experiment is given in reference (37).

The final step in ensuring the accurate time resolution of the experiment is to determine the amount of time it takes for the plasma to form as a means of determining the zero point offset from which all measurements were made. This is determined experimentally by viewing spectra at varying, early delays. The plasma turn on is characterized by a distinctly noticeable rise in the intensity of the signal. For the linear diode array/OMA experiments the zero point was determined to be 560 ns. Timing with ICCD was achieved through a direct line from the Q-switch output of the laser to the external trigger input on the camera. The zero point for the ICCD was determined to be 550 ns.

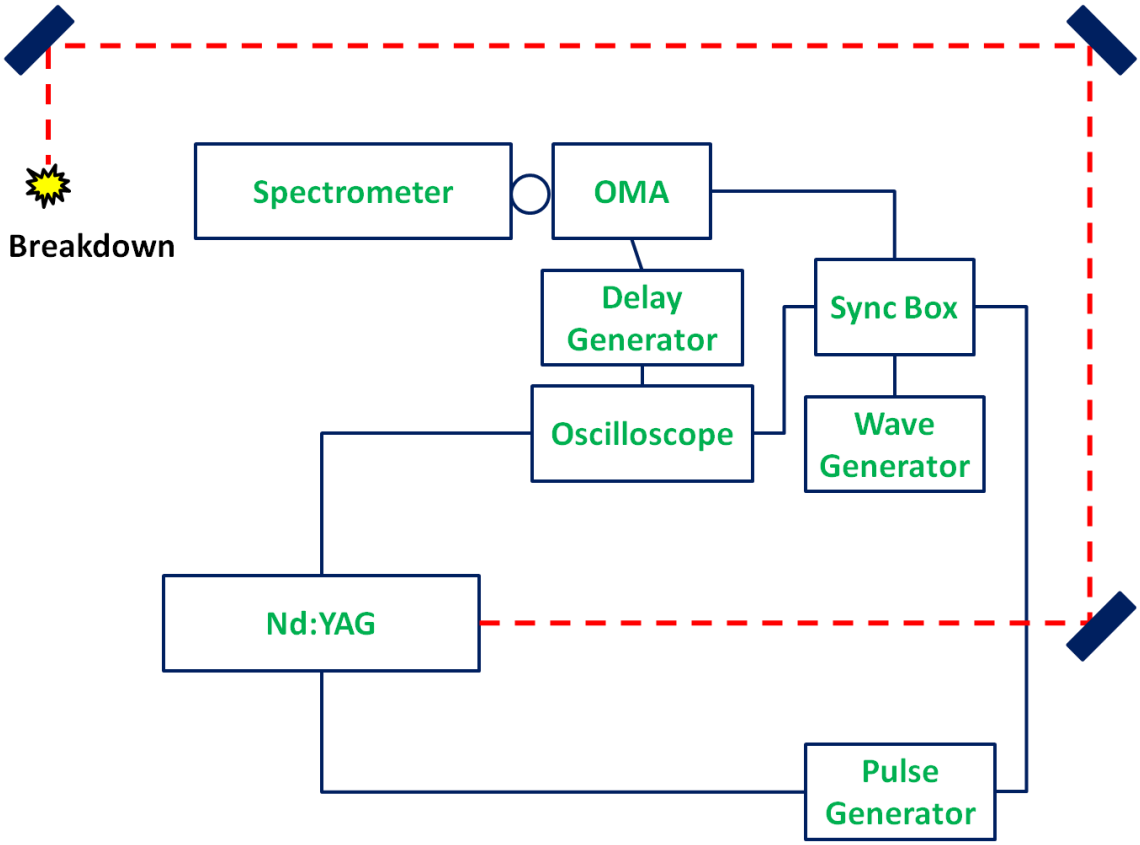

Figure 2. Block diagram of the apparatus used to achieve time resolution with the linear diode array experiments

After the spectra have been recorded, they must be calibrated for detector and background response. The dispersion of light emitted from the plasma is not expected to be linear. This is due to several factors including the age of the detector. This is accounted and corrected for by using standard calibrations lamps, such as a hydrogen gas lamp. The wavelength correction is determined by recording the known wavelength emissions of these standard lamps as a function of pixel position. A polynomial fit is then performed using least squares fitting to determine the wavelength as a function of pixel number. A cubic fitting function is sufficient to accurately correct the wavelength dispersion of a spectrometer-detector arrangement.

The wavelength region for the AlO $\Delta v=0$ (484-495nm) band is a particularly barren region with few spectral lines from calibration lamps. The wavelength calibration was performed with the use of the H_β line from an Oriel hydrogen lamp. A number of points to calibrate with were collected by shifting the spectrometer wavelength position by one nanometer and measuring the pixel number of the new position. This was repeated several times to gather enough points to perform a proper calibration. The linear diode was calibrated in this way, however the wavelength calibration of the ICCD requires a further step due to variations in the recorded pixel position along the height of the detector. Instead of calibrating each vertical track of interest, only the 500^{th} track was calibrated with the hydrogen lamp. This calibration was applied to all the vertical tracks, and corrections to the rest of the tracks were made by interpolating wavelengths from

theoretically calculated AlO spectra, which was possible since the pixel variation along the height of the detector was small.

Background sensitivity calibrations are performed to correct for the intensity response of the detector. As a detector is repetitively used its intensity response will diminish and will also naturally have regions that are more sensitive than others. The background sensitivity calibration is performed by measuring the spectra of a standard calibration lamp with a constant temperature output, such as a tungsten or halogen lamp, such that experimental spectra may be compared to a theoretical calculation of its thermal emission. The comparison is made by using a Nelder Mead fitting algorithm to fit the calibration spectrum to a theoretically calculated black-body curve with fit parameters of amplitude and offset. A fitted spectrum is then computed by determining the factor by which the experimental spectrum differs from the theoretical thermal spectrum and is applied to all experimental data. Each vertical track was calibrated from its own recorded intensity measurement from a standard calibration lamp. The calibration lamp used for the linear diode array experiments (Gamma Scientific RS-10A Spectral Radiance Head) had a temperature output of 2910 Kelvin and the standard calibration lamp used for the ICCD experiments (Ocean Optics DH-2000 Bal Halogen Source) had a standard output of 3000 Kelvin.

Chapter 3

Results

The goal of this study is accurately characterize the decay of aluminum laser-induced plasma. This was accomplished by studying atomic and molecular spectra emitted from the laser-induced plasma. Diatomic molecular AlO spectra are used at time delays later than 10 μs following formation of the laser-induced plasma to determine the temperature decay through comparisons to theoretically calculated AlO spectra. AlO measurements are also made along the plasma height with the use of the gated ICCD. At time delays earlier than 20 μs the electron number density is also inferred from measurements of the H_β line emission at 486.15 nm which were superimposed with measurements of AlO.

Diatomic AlO Results: Linear Diode Array

Diatomic molecular AlO data was collected with both the linear diode array and ICCD for the purpose of determining the temperature of the laser induced plasma as a function of time following the formation of the laser induced-plasma. The data set used to accomplish this goal covered a time delay range of 10 to 100 μs in 5 μs steps with gate widths of 5, 10, and 20 μs for delay ranges of 10-20, 20-100, and 70-100 μs, respectively. Different gate widths are used at different delays to acquire the best possible signal from the plasma. At early delays, the plasma emission is more intense and a smaller gate is needed as compared to later time delays when the plasma is less intense. The diatomic AlO spectra are analyzed by comparing the experimental spectra to theoretical

calculations of the diatomic spectra. The theoretical diatomic aluminum monoxide spectra used in this study were calculated from accurately compiled line strength tables.(38-42) A detailed description of how theoretical spectra for this study are calculated is provided in the appendix.

Comparisons between the experimental and theoretical spectra are made with the use of a Nelder-Mead minimization algorithm. The Nelder-Mead algorithm employs a downhill simplex fitting method to minimize user defined parameters of interest.(43,44) The downhill simplex method utilizes a geometric minimization technique in which a geometric construct known as a simplex is reduced in size by iteratively moving the positions of its vertices. The number of parameters determines the number of vertices for the created simplex and will be one more than the number of parameters. As an example, with a two parameter fit the simplex that is created is a triangle and in a three parameter fit a triangular tetrahedron is created. The initial simplex is created from user defined initial guesses for the parameters. An important aspect of using this algorithm is that rather than determining a global minimum for the input parameter, the algorithm returns the first local minimum it encounters. The determined local minimum may be closely considered a global minimum for a sufficiently small choice of the tolerance. In order to achieve decent results with this fitting method, the initial guesses used to seed the algorithm need to be within an error tolerance of the correct value; otherwise, the true minimum for one or all of the parameters may not be properly found.

The Nelder-Mead algorithm is chosen for its ability to include multiple fit parameters simultaneously as well as for its ability to allow variable baseline offsets. For this study, constant, linear, and quadratic baseline offsets were considered during fitting. The main parameters to be minimized were the temperature and the spectral resolution. Initially, the only varied parameter was the temperature, together with the baseline offset. In general the baseline offsets were slightly quadratic, with the coefficients for the linear and quadratic terms being an order of magnitude or smaller than the constant term. The spectral resolution of a particular spectrometer-detector arrangement is a determined parameter and was only varied in this study as a method to quantify the error associated with a particular inferred temperature. The resolution of a particular spectrum is dependent on a number of parameters such as the groove density of the installed grating, the amount of dispersion in the wavelength region of interest, the minimized slit width of the spectrometer, and the physical size of the pixels in a given detector. For the 1800 grooves/mm grating used with the linear diode array there was a dispersion of approximately 0.0175 nm per pixel which corresponds to a resolution of approximately 0.1 nm.

It was deemed that the best way to determine the resolution error was to overestimate the resolution by using a value of 0.09 nm and to underestimate it by using a value of approximately 0.125 nm. The value of 0.125 nm was determined by allowing the fitting program to find the minimized value of the resolution which varied from spectra to spectra. Fitting results for two data runs at time delays of 25 and 80 μs with gate widths

of 10 and 20 μs, respectively, are depicted in Figure 3 along with calculated residuals. The indicated temperatures in the figure are the corresponding temperature inferences for each experimental spectrum. The calculated residual shows that there are minor inaccuracies in the wavelength calibration from the appearance of rotational spectra in the calculated residual. Though the errors are within an acceptable margin, the differences support the use of varying the resolution as a method for error determination, as this inaccuracy will affect the determined resolution. This is also supported by considering the error from the extent of the slit. Though the two plots in Figure 3 appear to be qualitatively similar, the measurement made at 25 μs shows a larger continuum background in the residual and also has superposition atomic spectra (indicated on the figure) which qualitatively indicates a hotter plasma at the earlier time delay. Figure 4 shows the differences in the fitted experimental spectra with calculated residuals for the different resolutions used for diatomic molecular fitting for the same time delay of 60 μs. The temperature inference for each spectra is indicated on the plots. Rotational aspects are again present in the residuals of these plots. Close inspection of the residuals indicates that the 0.1 nm resolution fit tends to be the best resolution used as it minimizes the appearance of rotational characteristics in the residual as compared to the other resolutions.

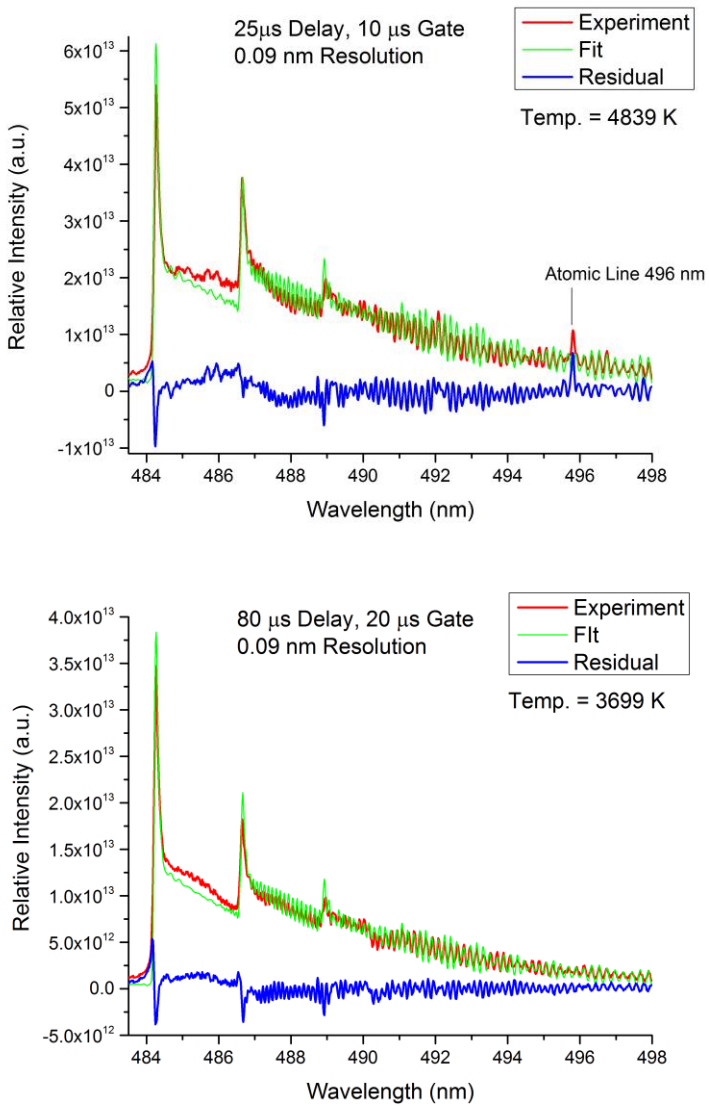

Figure 3. The experimental and fitted intensity graphs reveal the differences in fitted spectra at different time delays of 25 μs (top) and 80 μs (bottom) following laser-induced breakdown.

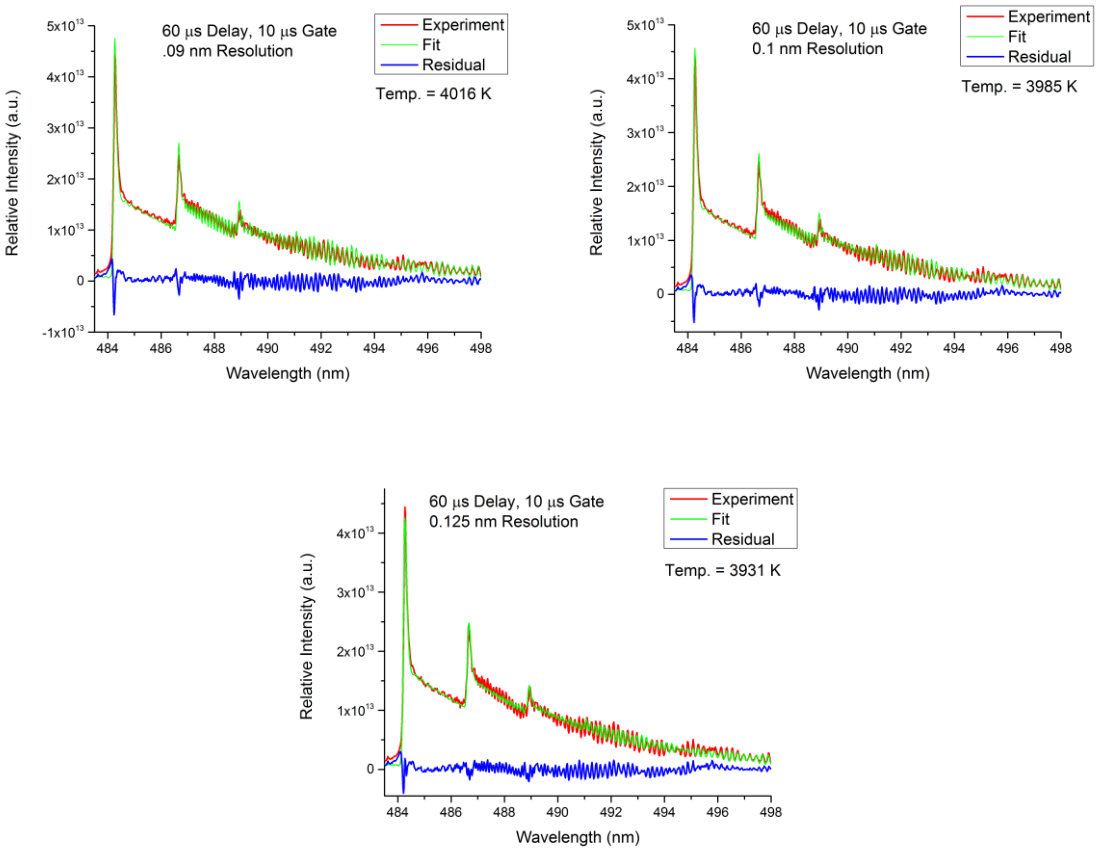

Figure 4. Experimental and fitted intensity showing the differences in fitted spectra for different spectral resolution parameters of 0.09 nm (top left), 0.1 nm (top right), and 0.125 nm (bottom center).

The error from varying the resolution of a particular fit amounted to be in the range of 40-70 Kelvin. This is not the only variable parameter capable of introducing errors. Variations in the baseline offset were also considered as a potential source of error. This was done by varying the coefficients of the linear and quadratic terms in the baseline offset up and down by an order of magnitude. This error typically amounted to a variation of 1-5 Kelvin from the initially inferred temperature values. Taken all together, the errors in the inferred temperature for a given spectral measurement amounted to be in the range of 45-75 Kelvin, with temperatures inferred at later times having values at the lower bound of the range. This is due, in part, to the decreased influence of the continuum radiation at later time delays. The inferred temperature results from each fit are collected in Table 1 along with the average temperature and the associated error in the temperature inference. There is one outlier in the inferred temperatures at a time delay of 10 μs. The large error associated with this measurement is due to the presence of H_β superposition emissions and arises from the varied resolution temperature inference. H_β superposition spectra are also observed for time delays of 15 and 20 μs; however, the errors in the temperature inferences do not reflect this due to the disappearance of the line with increasing time following breakdown. A plot of the temperature temporal dependence is recorded in Figure 5 and shows a temporal decay of the temperature. Included with Figure 5 is an exponential decay trend line illustrating the nature of the temperature decay through time and was obtained by fitting an exponential decay curve to all the linear diode array temperature results.

Table 2. Temperature inferences for each resolution considered with the linear diode array and the average reported temperature for each investigated time delay.

Delay Time (μs)	Gate Width (μs)	Temperature 0.09 nm Resolution (Kelvin)	Temperature 0.1 nm Resolution (Kelvin)	Temperature Varied Resolution (Kelvin)	Average Temperature (Kelvin)
10	5	5364	5314	4840	5173 ± 290
15	5	5113	5078	4983	5058 ± 73
20	5	4933	4899	4816	4883 ± 66
20	10	4625	4590	4510	4575 ± 65
25	10	4839	4805	4735	4793 ± 58
30	10	4765	4731	4657	4718 ± 61
35	10	4424	4392	4329	4382 ± 54
40	10	4477	4445	4375	4433 ± 57
45	10	4483	4452	4383	4439 ± 56
50	10	4212	4182	4128	4174 ± 48
55	10	4187	4154	4075	4138 ± 63
60	10	4016	3985	3931	3978 ± 48
65	10	4268	4236	4159	4221 ± 61
70	10	4099	4067	3976	4047 ± 69
75	10	4223	4191	4112	4175 ± 63
80	10	4044	4014	3922	3993 ± 69
85	10	4082	4050	3963	4031 ± 67
90	10	3629	3598	3538	3588 ± 51
95	10	3828	3797	3742	3789 ± 49
100	10	3899	3869	3817	3862 ± 46
70	20	3651	3619	3540	3604 ± 63
75	20	3816	3781	3685	3760 ± 72
80	20	3699	3668	3591	3653 ± 62
85	20	3811	3780	3711	3767 ± 56
90	20	3990	3960	3910	3953 ± 46
95	20	3901	3873	3836	3870 ± 40
100	20	3879	3849	3803	3844 ± 43

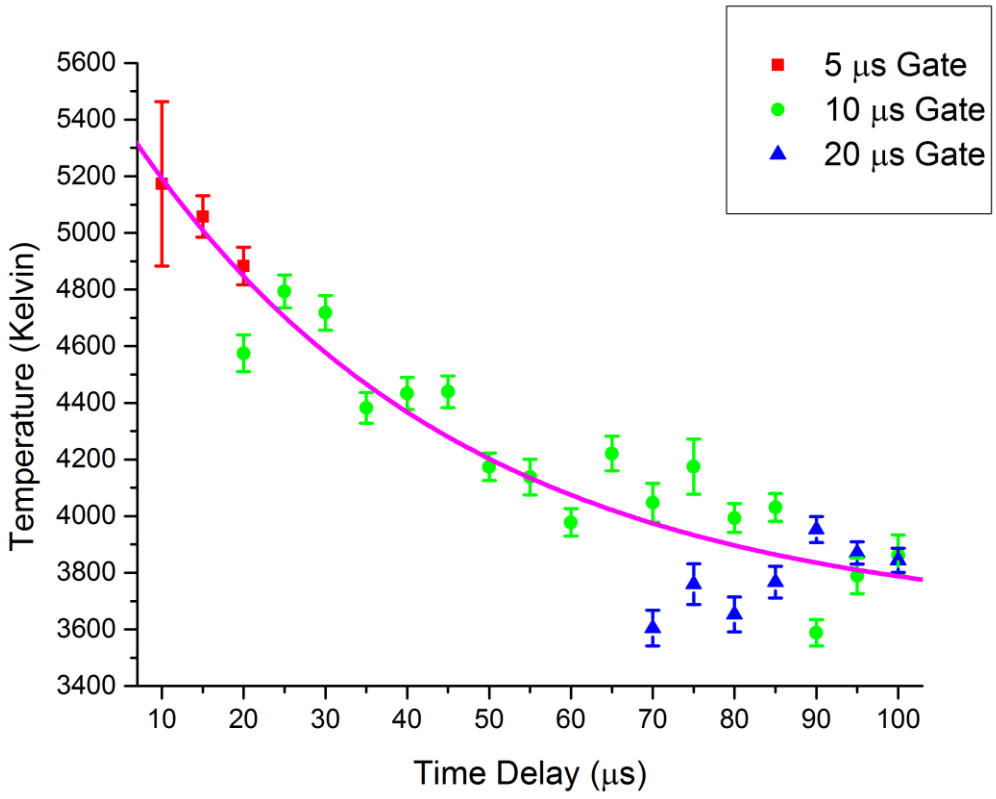

Figure 5. Inferred temperatures and associated errors as a function of time delay. The purple trend line shows the temporal decay of the temperature.

The temperature inference results at early time delays are found to be higher than those inferred at later delay times. This trend is observed in the data collected with 5 and 10 μs gate widths. The temperature decays from a value of 5173 ± 290 Kelvin at 10 μs to a value of 3588 ± 51 Kelvin at 90 μs following breakdown. After this time there is an apparent rise in the temperature to 3862 ± 46 Kelvin at 100 μs following breakdown. This is mirrored with the data collected with a 20 μs gate width as the temperature increases from 3604 ± 63 Kelvin at 70 μs to 3844 ± 43 Kelvin at 100 μs. Though this temperature rise is clearly apparent in the 20 μs gate width data, it is weakly present in the 10 μs gate width data and could not be present due to shot to shot variations in laser-induced breakdown spectra from the temperature inferred such as the temperature inference at 90 μs. An argument could be made that the temperature inference at 100 μs is greater than the temperature inferred at 95 μs. Though this is true, the relative closeness of the two temperatures indicate more properly a plateau in the temperature rather than a rise in the temperature. This temperature rising effect is clearly present in the 20 μs gate width data even when shot to shot variations are considered, such as at 75 and 90 μs time delays. This also suggests that the temperature eventually plateaus for time delays later than 95 μs which is congruent with the results from the 10 μs gate data. A possible cause for this behavior is due to combustion of aluminum particles present in the plasma plume.

Diatomic AlO Results: ICCD

Diatomic molecular AlO spectra were collected with the gated ICCD for the purpose of investigating the temperature dependence along the height of the laser-

induced plasma. In this investigation only one time delay was considered, 60 μs with a 6 μs gate width. Spectra were collected along the height of the plasma using all 1024 vertical pixels on the ICCD detector. To investigate the behavior of the temperature dependence along the height of the plasma, spectra from tracks 100-700 in 100 track intervals were calibrated and analyzed. Errors in the inferred temperature were again found by varying the offset and resolution. Figure 6 is an image of the AlO spectra as seen by the detector of the ICCD and Figure 7 a plot of the inferred temperatures as a function of vertical track position. The temperature inferences from each resolution, the average temperature and its associated error are collected in Table 2. Due to the decrease in resolution from using non-optimal plasma conditions and ICCD settings, there are significantly larger errors in the inferred temperatures. This also resulted in a significantly poorer resolution of approximately 0.3 nm.

The errors in the temperature were estimated in a similar fashion as the linear diode array experiments. Values of 0.4 and 0.2 nm were used to over- and under-estimate the spectral resolution. These errors amounted to be in the range of 230 to 275 Kelvin. The results of the temperature analysis also returned unexpectedly high temperatures that did not agree with the previously determined temperatures from the linear diode array experiment or from temperatures found in the literature. This is again likely due to the quality of the signal collected with the ICCD which could be caused by

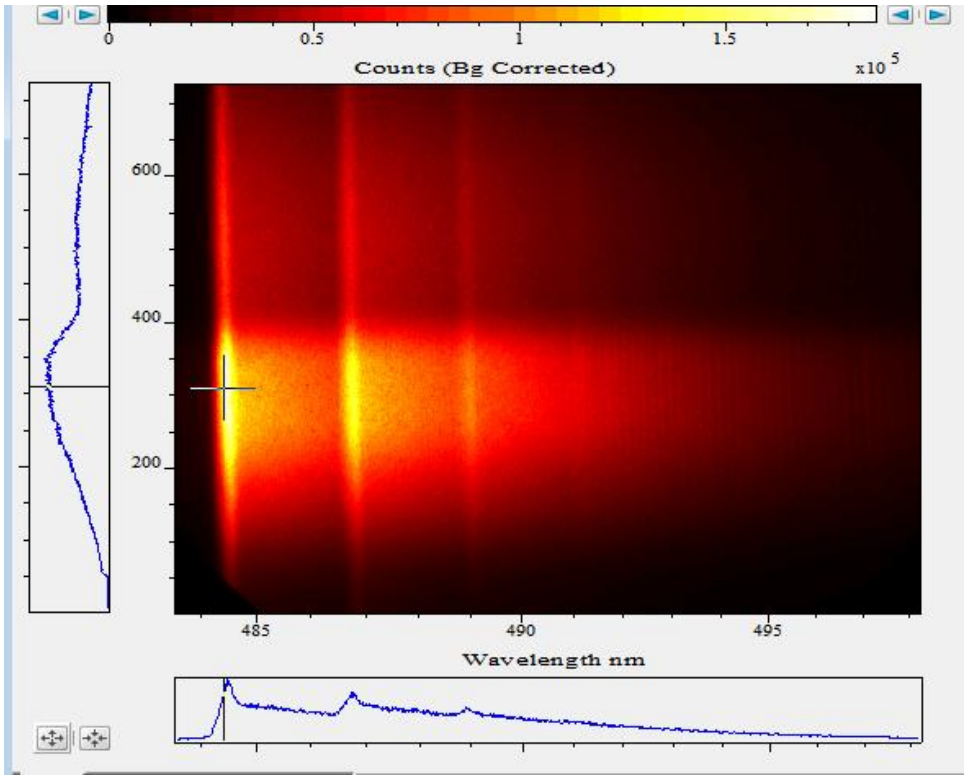

Figure 6. Raw AlO spectra recorded with the ICCD indicating an increase in the amount of AlO above the edge of the plasma. Pseudo-coloring is applied as indicated by the bar at the top of the figure. On the bottom is a plot of the intensity across the width of the detector for a single vertical track. The plot to the left of the image shows the intensity gradient along the height of the detector at a specific pixel position.

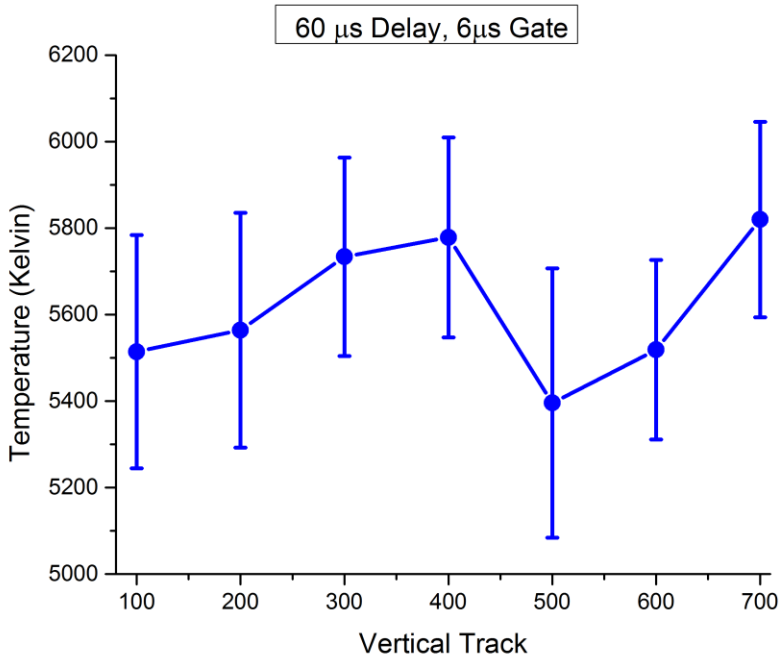

Figure 7. Inferred temperatures and associated errors along the height of the ICCD, indicating an increase in the temperature above the plasma edge.

Table 3. Temperature inferences for each resolution considered and the average temperature for each considered vertical track along the height of the plasma.

Vertical Track Position	Temperature 0.2 nm Resolution (Kelvin)	Temperature Varied Resolution (Kelvin)	Temperature 0.4 nm Resolution (Kelvin)	Average Temperature (Kelvin)
100	5818	5422	5303	5514 ± 275
200	5849	5535	5309	5564 ± 276
300	5977	5703	5521	5734 ± 235
400	6023	5751	5562	5779 ± 236
500	5754	5242	5191	5396 ± 315
600	5728	5516	5312	5519 ± 213
700	6059	5791	5610	5820 ± 230

using too many vertical tracks. Despite this concern, this analysis did return information in regards to the temperature behavior of the plasma along its vertical axis. These results indicate that there is a rise in the temperature until a peak is reached between tracks 300 and 400. The temperature then falls off until a minimum is reached at track 500. This represents the plasma itself which is expected to be hotter at its center as compared to its edges. The temperature increases again after falling off at the edge of the plasma. The increased temperature as determined from the AlO molecule's spectral signal is likely due to the presence of aluminum particles that may be undergoing combustion in a plume that is above the plasma. This is also supported by the increased intensity of the AlO signal as seen in the ICCD image in Figure 6.

Atomic Spectra Results: H_β Superposition Spectra

Measurements of diatomic molecular AlO at time delays earlier than 20 μs show superposition emission spectra of AlO with H_β and carbon atomic emissions. Figure 8 depicts this for a time delay of 10 μs where the atomic emissions are marked and clearly visible in the calculated residual. Stark broadening of the emissions of the H_β line at 486.15 nm may be used to infer the electron number density of the plasma with the use of the theories of Konjević and Oks.(15,18,19) Also visible are a carbon emission line at 493.2 nm and another atomic emission line at 496.7 nm that could possibly be carbon or titanium, which is present in the aluminum alloy that was used.

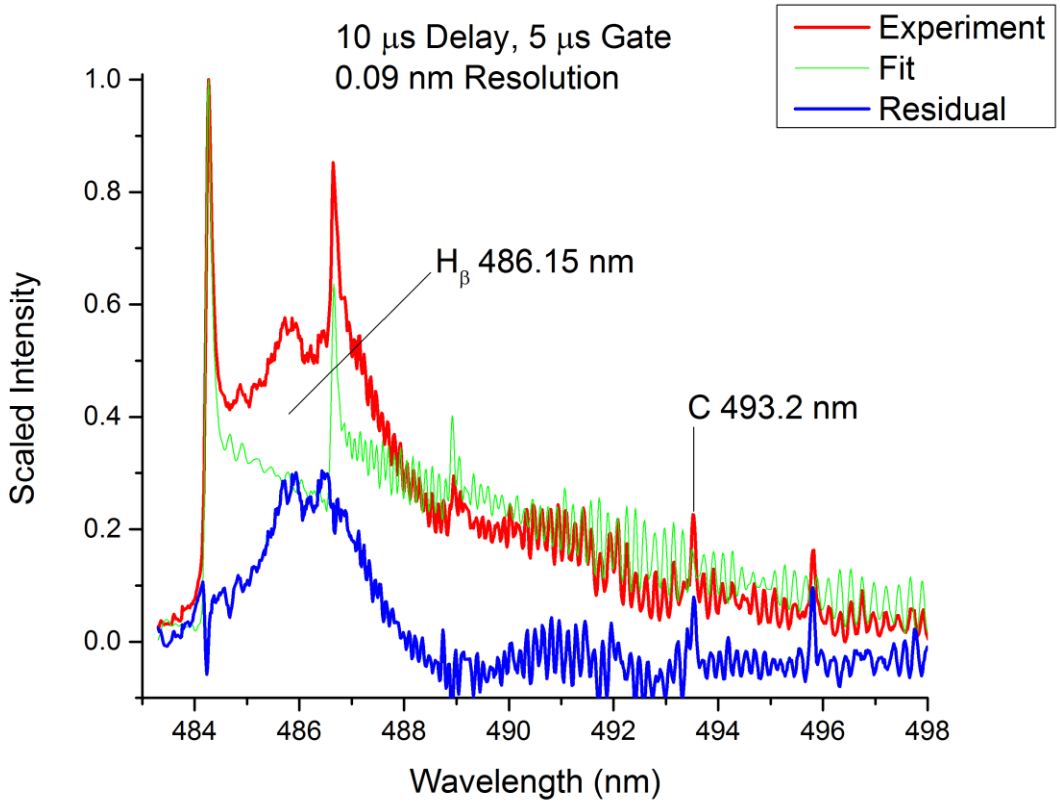

Figure 8. Collected superposition spectra from the laser ablated aluminum sample at a time delay of 10 μs. This illustrates H_β emissions near 486 nm and a carbon emission line near 493 nm. Also seen is an unknown atomic emission line near 496 nm.

In order to infer the electron number density, the width of the line due to Stark broadening must be known. The line widths are determined by fitting a Lorentzian line profile to the H_β emission. It is assumed that the broadening of this line is primarily due to Stark effects in the hydrogen atom. The errors in the associated line width will primarily be due to the influence of the slit width and the accuracy of the Lorentzian fitting. N_e values were inferred using both the empirical formula of Konjević and the convergent theory of Oks. In order to infer the electron density with the theory of Oks, N_e vs. H_β line width experimental results published by Parigger *et al.* (10) were fit with an exponential function. Figure 9 combines the results of this analysis, and the figure also includes the fitted exponential function of the N_e value as a function of the determined line width of the H_β emission line where *w* in the function indicates the line width in angstroms. Fitting of this kind was also completed in a study H_α and H_β emissions in air laser-induced plasmas.(20) The results of the line width fitting and accompanying N_e inferences are collected in Table 3 and show both inferred N_e values for Oks' and Konjević's theories as well as the accompanying error. Figure 10 shows an example H_β spectra that was fit from the residual of the spectra shown in Figure 8 and Figure 11 is a plot of the N_e values inferred from both theories as a function of the fitted line width. The H_β emission spectra in Figure 9 have double peak structures present which is also indicated. This double peak is not due to affects of the superposition with AlO spectra but also results from Stark effects. Though not considered in this work, the indicated peak

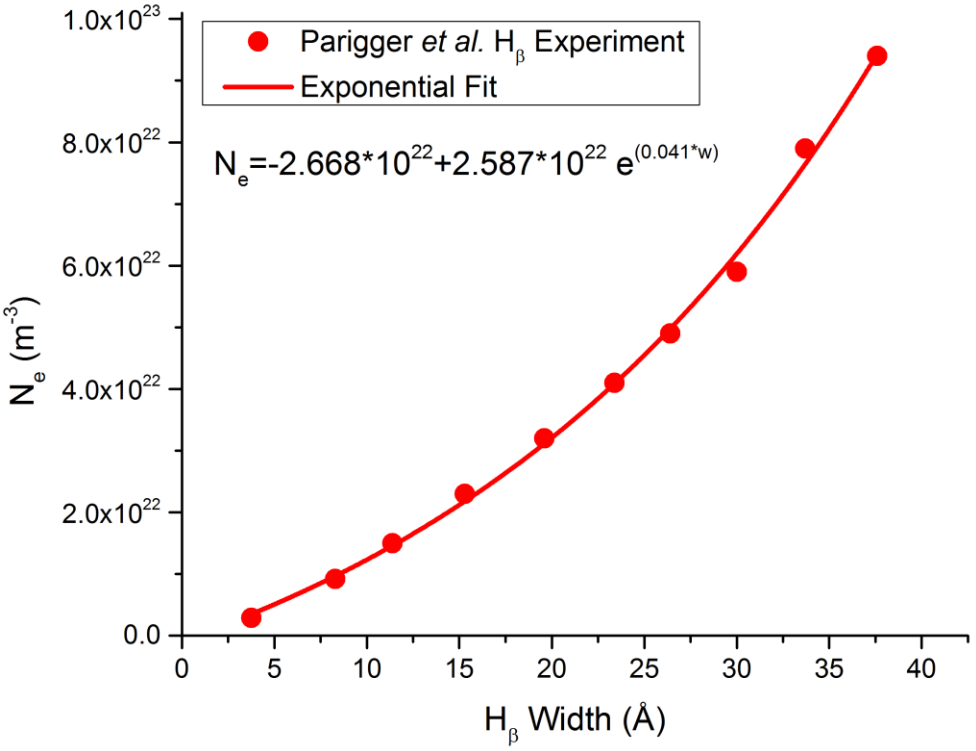

Figure 9. Plot of fitting results of pure hydrogen experiments used to determine N_e values along with the determined exponential function.

Table 4. Line width results from Lorentzian fitting and accompanying inferred N_e values using the theory of Oks and the empirical formula from Konjević.

Delay Time (μs)	Inferred Line Width (nm)	Konjević Empirical N_e (10^{22} m^{-3})	Oks Convergent N_e (10^{22} m^{-3})
10	2.53 ± 0.21	4.32 ± 0.54	4.59 ± 0.45
15	2.26 ± 0.24	3.69 ± 0.60	3.91 ± 0.39
20	1.94 ± 0.36	2.91 ± 0.82	3.15 ± 0.31

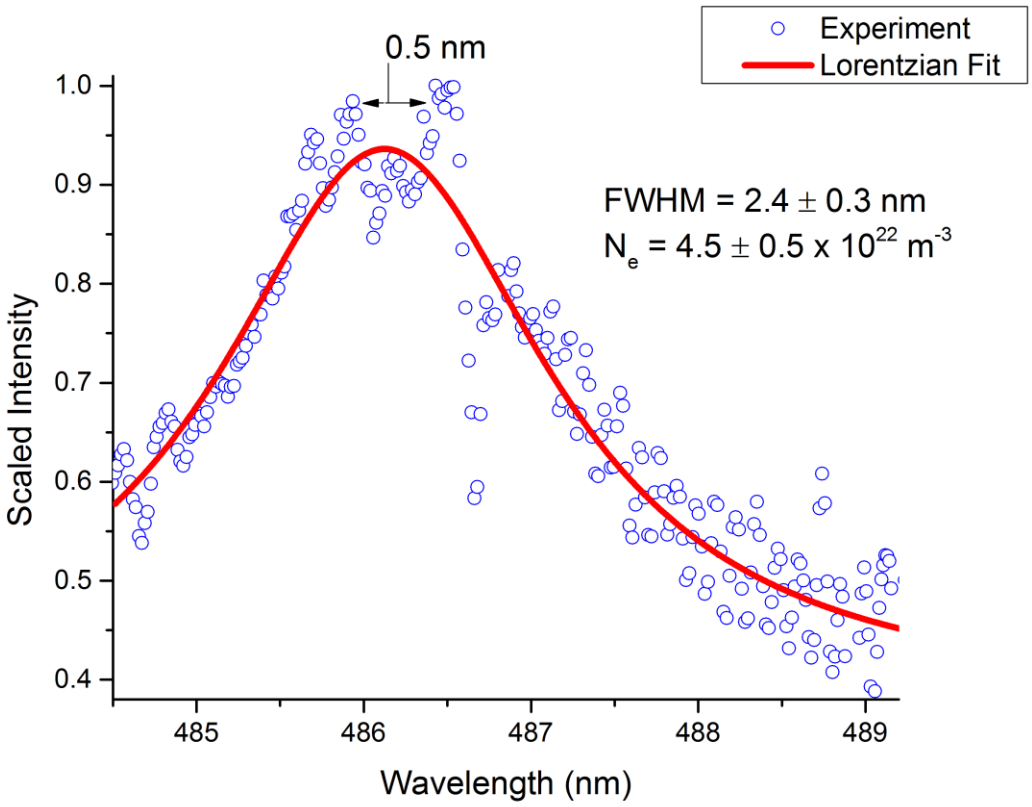

Figure 10. Fitted H_β spectra from the measured AlO residual at a 10 μs time delay indicating the inferred line width and electron number density. The sudden dip in the residual near 486 nm is due to the subtraction of the intensity fit from the experimental spectra and occurs near the 1-1 vibrational peak.

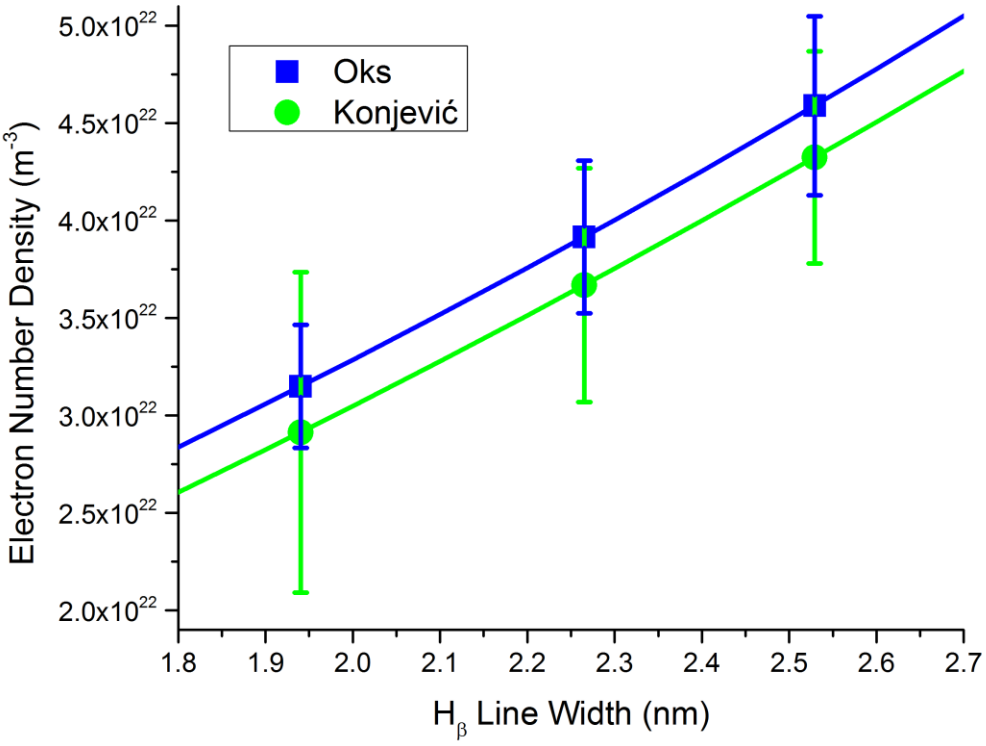

Figure 11. Plot of inferred N_e results vs. line width using both the theories of Oks and Konjević.

separation of approximately 0.5 nm may be used as another method of inferring the electron number density of the laser-induced plasma.(15) Also included with Figure 10 is the fitted exponential function used to infer N_e from Oks' theory. Using both theories, the N_e is inferred to be on the order of 4.5×10^{22} m^{-3} at 10 μs and decreases to approximately 3×10^{22} m^{-3} at 20 μs following breakdown as the width of the H_β line decreases from approximately 2.5 nm to 1.9 nm. Atomic lines are expected to narrow as the plasma decays through time. This leads to the expected result of a decaying N_e as a function of increasing time delay following laser induced breakdown. In comparison to other known values of N_e in aluminum laser-induced plasmas of 10^{23} m^{-3} at time delays of 1 μs following breakdown, the inferred values in this study at later time delays are appropriate estimates for the plasmas generated.

Chapter 4

Discussion

Both the temperature and the electron density are expected to decay as a function of increasing time delay following initiation of the laser-induced plasma. Both of these trends have been observed in the inferred temperatures and N_e in this study. In regards to the temperatures inferred with measurements made with the linear diode array, the results appear to be in good agreement with values available in the literature of 4250 and 4000 Kelvin at a time delay of 50 μs following breakdown.(28-30) The temperature inferred from this study at that time delay was 4174 ± 48 Kelvin. In this scope, the temperatures that are inferred at earlier and later time delays than 50 μs should provide an accurate characterization of the temporal behavior of the temperature of the laser-induced plasma. The inferred electron densities in this study of 3 to 4.5×10^{22} m^{-3} at 10 to 20 μs delays are also in decent agreement with previously determined values of 10^{23} m^{-3} for a one μs delay (30) when considering that the electron density is expected to decay through time. The decay is also expected to be more rapid early in the decay in the plasma and slow as the time delay is increased from hundreds of nanoseconds to tens of microseconds. Given the errors in the reported N_e values, the inferred N_e provide a good characterization of the number of free electrons in the laser-induced plasma.

The errors in the inferred temperatures were found by considering variations introduced by the fitting method. In a previous study of an aluminum laser-induced plasma (31) in which the same apparatus was used and the errors were determined using

similar methods as this study, the errors were almost twice as large as those in this study. One would expect to have the margin of error be in the ± 100 Kelvin range to account for both the systematic error introduced from the fitting algorithm and errors from shot to shot variations since it is unlikely multiple spectra produced from a single laser-induced breakdown event will be exactly the same every time a measurement is made. The larger errors of approximately 100 Kelvin could possibly include shot to shot variations in the spectra and hence the inferred temperatures. As the temperature results are, the results from the linear diode array experiments do not consider shot to shot variations. Considering this error will likely increase most of the determined errors by as much as 40 to 50 Kelvin. Further, only a few of the possible sources of error with the fitting algorithm have been included in the error determination. The effects of the temperature used to seed the algorithm, the tolerance, and fit range should all be included in further studies. In all, a complete characterization of the errors in the inferred temperatures should consider all the effects from the fitting algorithm and shot to shot variations and the reported results from this study should be considered in this context.

The temperature inferences both from the linear diode array and ICCD experiments appear to suggest that combustion is occurring at late time delays in the evolution of the laser-induced plasma in this study. Combustion can occur as nano- and micro-sized particles are produced when the target material is laser ablated. The direction in which these particles travel is dependent on the geometry of a particular experimental arrangement. In the current study, in which the laser radiation is incident vertically

downward on the aluminum target, a large number of these particles would be expected to be above the laser-induced plasma. Given that the combustion temperature of aluminum is approximately 2750 Kelvin, it is reasonable to expect that at later time delays, after the plasma has decayed enough, that combustion of aluminum particles available in and around the plasma will begin to dominate the observed radiation emissions.

At early time delays plasma radiation processes are expected to be dominant due to continuum radiation process. The temperature rising trend observed with the linear diode array support the presence of combustion in the laser-induced plasma as the temperature of the plasma is expected to increase as combustion begins to occur. Further, it is expected that combustion would not be observable until much later, possibly after 80 μs as observed in this study. Though the temperatures inferred from the ICCD appear to be much larger than the accepted values, the temperature trend along the height of the detector is valid, which shows that there is an increase in the temperature above the edge of the plasma. Though these results are encouraging for the presence of combustion, more positive results would be required to make a declaration that combustion is present in the aluminum laser-induced plasma and more measurements should be made to check for the repeatability of the results presented in this work.

Chapter 5

Conclusions

The goal of this study was to determine the temporal decay of the plasma produced near the surface of an aluminum target following laser ablation with nanosecond laser radiation pulses. This was achieved with time resolved LIBS. Spectral measurements from the laser-induced plasma were made with an intensified linear diode array and an ICCD which was used to collect spatially as well as temporally resolved spectra along the height of the laser-induced plasma. The collected spectra were properly calibrated and the AlO emissions were analyzed through comparisons to theoretically calculated spectra with the use of a Nelder-Mead algorithm. Temperatures inferred from linear diode array measurements show that the temperature of the plasma decreases over time from a value of 5173 ± 290 Kelvin at 10 μs to a value of 3588 ± 51 Kelvin at 90 μs. At time delays later than this, data collected with the 10 μs gate suggests the temperature of the plasma plateaus to a value of 3862 ± 46 Kelvin. This is mirrored in the data collected with a 20 μs gate in which the temperature increases from 3604 ± 63 Kelvin at 70 μs to 3844 ± 43 Kelvin at 100 μs. All of the inferred temperatures from the linear diode array measurements seem to be in good agreement with available temperature results in the literature.

Temperatures were also inferred along the height of the plasma from measurements made with the ICCD. These temperature inferences indicate that the plasma is hottest at its center, and the temperature falls of towards the edges. The

temperature increases above the plasma in what can be called the plasma plume. The increase in temperature at later time delays, the observation of H_β and carbon superposition spectra, and the increase in temperature above the plasma, all support combustion in the aluminum laser-induced plasma. In the immediate future these results should be corroborated and thoroughly checked for their repeatability.

Observations of atomic H_β spectra superimposed on diatomic AlO spectra at time delays earlier than 20 μs following the formation of the plasma were made. Line widths of the H_β spectra were inferred by fitting Lorentzian line profiles to the processed H_β spectra. The determined line widths were used with the empirical formula of Konjević and the convergent theory of Oks to infer the electron number density of the laser-induced plasma at times preceding 20 μs following initiation of the plasma. Using both theories the inferred density is found to be on the order of 4.5×10^{22} m^{-3} and decreases to a value of approximately 3×10^{22} m^{-3} over a period of 10 μs which is in agreement with published values available in the literature in regards to aluminum laser-induced plasma.

Recommendations for Future Work

The work completed in this study represents the ground work in defining the parameters that characterize aluminum laser-induced plasma. Though this work has successfully determined the temperature of the plasma as a function of time delay, more measurements with the ICCD will only help to support the results of this work. More ICCD measurements with more ideal camera settings and plasma conditions will also be advantageous in better determining the temperature behavior along the height of the

plasma. In the immediate future, this should be addressed. This study also considered errors introduced from the fitting algorithm. Though these were accounted for in an appropriate manner, future works will seek to better quantify this effect by considering the effect of other variable parameters such as the initial guess of the temperature and the value of the tolerance level. A thorough investigation of early time delays on the order of hundreds of nanoseconds to a few microseconds following plasma formation should also accompany any further studies at later time delays to infer the temperature and electron number density and give a complete profile of the aluminum laser-induced plasma through time.

Also of interest are studies of the depth of the plasma which are obtainable through de-convolution of the ICCD measured spectra with the use of Abel and Radon transform techniques. The Abel and Radon transforms are computational methods in which spectroscopic data are de-convolved to determine the true intensity of a spectral signal. This requires an absolute calibration of the spectrometer-detector arrangement. The goal of the Abel transform is use the recorded intensity at some position, $I(z)$, to determine the local emission coefficient as a function of position, which may be used to determine a number of plasma parameters including electron number densities and concentrations of specific elements, such as aluminum, within the plasma. Applications of Abel transforms are limited as the transform requires the assumption of an axially cylindrical, symmetric plasma and requires that the plasma be optically thin. This represents idealized laser-induced plasma. For situations where the plasma may be

optically dense and not symmetric, as is the case when laser ablating a solid target due to imperfections on the surface of the sample, one may use the Radon transform, which is a generalization of the Abel transform. The Radon transform assumes no symmetry and that the intensity, $I(z,\alpha)$, varies as a function of radial and angular position. When the intensity is the same for a position and a position offset by some angle, $I(z,\alpha)= I(z)$, the Radon transform reduces to the Abel transform.

Further, work in the field of aluminum combustion could consider applications of aluminum plasma characterizations as a diagnostic tool given the encouraging results that combustion is present in the laser-induced plasma. Of specific interest to research in this field is determining the interaction of aluminum particles with the surrounding flame. One of the key parameters of interest in studying this interaction is the temperature of the aluminum particle and the surrounding flame. This has been previously studied in aluminized flames (45,46) and aluminized solid propellant flames.(47-51) Studies of aluminum laser ablation are advantageous for combustion applications due to the cost and safety concerns associated with combustion experiments that do not exist with laser-induced plasma studies. As well, studies of laser ablation of an aluminum target in different atmospheres are of interest for studies of aluminum combustion diagnostics. In particular, nitrogen, nitrogen-oxygen mixtures, and hydrogen atmospheres should be considered.

List of References

1. C.G. Parigger Atomic and molecular emissions in laser-induced breakdown spectroscopy. Spectrochim. Act. B. 2013; 79:4-16.

2. L.J. Radziemski and D.A. Cremers, editors. Laser-induced plasmas and applications. New York: Marcel Dekker; 1989.

3. A.W. Miziolek, V. Palleschi, and I. Schechter, editors. Laser induced breakdown spectroscopy. New York: Cambridge University Press; 2006.

4. J.P. Singh and S.N. Thakur, editors. Laser induced breakdown spectroscopy. New York: Elsevier Science; 2007.

5. F.C. De Lucia, R.S. Harmon, K.L. McNesby, R.J. Winkel, and A.W. Miziolek. Laser-induced breakdown spectroscopy analysis of energetic materials. Appl. Opt. 2003; 42:6148-6152.

6. H. Wiggenhauser, D. Schaurich, and G. Wilsch. LIBS for non-destructive testing of element distributions on surfaces. NDT and E International. 1998; 31:307-313.

7. D.E. Cremers and L. J. Radziemski. Handbook of laser-induced breakdown spectroscopy. New York: John Wiley; 2006.

8. R.C. Wiens, S. Maurice, J. Lasue, O. Forni, R.B. Anderson, S. Clegg, et al. Pre-flight calibration and initial data processing for the ChemCam laser-induced breakdown spectroscopy instrument on the mars science laboratory rover. Spectrochim. Act. B. 2013; 82:1-27.

9. C.S. Chen, B.Y. Man, D. Liu, X. Song, and X.J. Chen. Investigation of Ti III line broadening in a laser-induced plasma. J. Phys. B: At. Mol. Opt. Phys. 2013; 46:1570-1574.

10. V.N. Ochkin. Spectroscopy of low temperature plasma. Mörlenbach, DEU: Wiley-VCH; 2009.

11. H.J. Kunze. Introduction to plasma spectroscopy. New York: Springer; 2009.

12. I.B. Gornuskin, S. Merk, A. Demidov, U. Panne, S.V. Shabanov, B.W. Smith, et al. Tomography of single and double pulse laser-induced plasma using radon transform technique. Spectrochim. Act. B. 2012; 76:203-213.

13. Y.P. Kandel. An experimental study of H-balmer lines in pulsed laser plasma. B.A. Thesis with honors. 2009; Wesleyan University, Middletown, CT.

14. B.H. Brandsen and C.J. Joachain. Physics of atoms and molecules, second edition. New York: Prentice Hall; 2003.

15. C.G. Parigger, D.H. Plemmons, and E. Oks. Balmer series H-beta measurements in a laser-induced hydrogen plasma. Appl. Opt. 2003; 42:5992-6000.

16. C.G. Parigger, J.W.L. Lewis, and D.H. Plemmons. Electron number density and temperature measurement in a laser-induced hydrogen plasma. J. Quant. Spectrosc. Rad. Transf. 1995; 53:249-255.

17. J.F. Kielkopf. Spectroscopic study of laser-produced plasmas in hydrogen. Phys. Rev. E. 1995; 52:2013-2024.

18. B. Miles and J. Cortes. Subsurface heavy-metal detection with the use of laser-induced breakdown spectroscopy (LIBS) penetrator system. Field Anal. Chem. Tech. 1998; 2:75-87.

19. S.C. Jantzi and J.R. Almirall. Characterization and forensic analysis of soil samples using laser-induced breakdown spectroscopy (LIBS). Anal. Bioanal. Chem. 2011; 400:3341-3351.

20. N. Konjević, M. Ivković, and N. Sakan. Hydrogen balmer lines for low electron number density plasma diagnostics. Spectrochim. Act. B. 2012; 76:16-26.

21. H.R. Griem. Spectral line broadening by plasmas. New York: Academic; 1974.

22. H.R. Griem. Principles of plasma spectroscopy. Cambridge: Cambridge University Press; 1997.

23. Y. Ispolatov and E. Oks. A convergent theory of stark broadening of hydrogen lines in dense plasmas. J. Quant. Spectrosc. Rad. Transf. 1994; 51:129-138.

24. J.E. Touma, E.A. Oks, A. Alexiou, and A. Derevianko. Review of the advanced generalized theory for stark broadening of hydrogen lines in plasmas with tables. J. Quant. Spectrosc. Rad. Transf. 2000; 53:543-571.

25. C.G. Parigger, L.D. Swafford, A.C. Woods, D.M. Surmick, and M.J. Witte. Asymmetric hydrogen-beta electron density diagnostics in laser-induced plasma. Submitted to Spectrochim. Act. B. 2014.

26. J.O. Hornkohl, C.G. Parigger, and J.W.L Lewis. Temperature measurements from CN spectra in a laser-induced plasma. J. Quant. Spectrosc. Rad. Transf. 1991; 46:405-411.

27. C.G. Parigger, A.C. Woods, and J.O. Hornkohl. Analysis of time-resolved atomic hydrogen balmer and molecular carbon spectra. Appl. Opt. 2012; 51: B1-B6.

28. A.C. Woods, C.G. Parigger, and J.O. Hornkohl. Measurements and Analysis of titanium monoxide spectra in a laser-induced plasma. Opt. Lett. 2012; 37:5139-5141.

29. A. Colibaba-Evulet, A. Singhal, and N. Glumac. Detection of AlO and TiO by laser-induced fluorescence in powder synthesis flames. Combust. Sci. and Tech. 2000; 157:129-139.

30. M. Sabsabi and P. Cielo. Quantitative analysis of aluminum alloys by laser-induced breakdown spectroscopy and plasma characterization. Appl. Spectrosc. 1995; 49:499-507.

31. A.K. Rai, F. Yueh, and J.P. Singh. et al. Laser-induced breakdown spectroscopy of molten aluminum alloy. Appl. Opt. 2003; 42:2078-2084.

32. T.N. Piehler, F.C. DeLucia, C.A. Munson, B.E. Homan, A.W. Miziolek, and K.L. McNesby. Temporal evolution of the laser-induced breakdown spectroscopy spectrum of aluminum metal in different bath gases. Appl. Opt. 2005; 44:3654-3660.

33. J.M. Lightstone, J.R. Carney, C.J. Boswel, and J. Wilkinson. Time-resolved spectroscopic measurements of aluminum oxidation in a laser ablation event. AIP Conf. Proc. 2007; 955:1255-1258.

34. C.G. Parigger, J.O. Hornkohl, and L. Nemes. Measurements of aluminum and hydrogen microplasma. Appl. Opt. 2007; 46:4026-4031.

35. C.G. Parigger. Measurements of laser-induced plasma and optical breakdown spectra of aluminum. AIP Conf. Proc. 2006; 874:101-111.

36. D.M. Surmick and C.G. Parigger. Aluminum monoxide emission measurements in laser-induced plasma. Accepted. Appl. Spectrosc. 2014.

37. C.G. Parigger, A.C. Woods, M.J. Witte, L.D. Swafford, and D.M. Surmick. Measurement and analysis of atomic hydrogen and diatomic molecular AlO, C_2, CN, and TiO spectra following laser-induced optical breakdown. J. Vis. Exp. 2014; 84.

38. I.G. Dors, C. Parigger, and J. Lewis. Spectroscopic temperature determination of aluminum monoxide in laser ablation with 266-nm radiation. Opt. Lett. 1998; 23:1778-1780.

39. C.G. Parigger and J.O. Hornkohl. Computation of AlO $B^2\Sigma^+ \rightarrow X^2\ \Sigma^+$ emission spectra. Spectrochim. Act. A. 2011; 81:404-411.

40. J.O.Hornkohl, C.G. Parigger, and L. Nemes. Diatomic Hönl-London factor computer program. Appl. Opt. 2005; 44:3686-3695.

41. C.G. Parigger and J.O. Hornkohl. Diatomic molecular spectroscopy in laser-induced breakdown plasma. Int. Rev. Atom. Mol. Phys. 2010; 1:25-43.

42. J.O. Hornkohl, L. Nemes, and C.G. Parigger. Spectroscopy C-2 and CX. In: L. Nemes and S. Irle, editors. Spectroscopy, dynamics and molecular theory of carbon plasmas and vapors, advances in the understanding of the most complex high-temperature elemental system. Singapore: World Scientific; 2011. p. 113-169.

43. J.A. Nelder and R. Mead. A simplex method for function minimization. The Comp. J. 1965; 7:308-313.

44. J.C. Lagarias, J.A. Reeds, M.H. Wright, and P.E. Wright. Convergence properties of the nelder-mead simplex method in low dimensions. SIAM J. Optim. 1998; 9:112-147.

45. D.M. Surmick and C.G. Parigger. Analysis of aluminum monoxide emission spectra in a simulated solid rocket propellant flame. In Bulletin of the American Physical Society: 80th Meeting of the Southeastern Section of the American Physical Society. 2013; Bowling Green, KY: paper DD11.

46. A. Huag, B.C. Hogan, A.B. Donaldosn, C.G. Parigger, and D.M. Surmick. Simulating and modeling rocket propellant plume using an aluminum powder fed oxyacetylene torch. Western States Sections of the Combustion Institute Fall Meeting. 2013; Ft. Collins, CO.

47. D.M. Surmick, C.G. Parigger, A.C. Woods, A.B. Donaldson, J.L. Height, and W. Gill. Analysis of emission spectra of aluminum monoxide in solid propellant flame. Int. Rev. Atom. Mol. Phys. 2012; 3:137-151.

48. C.G. Parigger, A.C. Woods, D.M. Surmick, A.B. Donaldson, and J.L. Height. Aluminum flame temperature measurements in solid propellant combustion. Appl. Spectrosc. 2014; 68:362-366.

49. C.G. Parigger, D.M. Surmick, A.C. Woods, A.B. Donaldson, and J.L. Height. Measurement and analysis of aluminum monoxide emission spectra. 8th US National Meeting of the Combustion Institute. 2013; Park City, UT: paper 305.

50. D.M. Surmick, A.C. Woods, C.G. Parigger, J. Height, A.B. Donaldson, and W. Gill. Spectroscopy of aluminum monoxide in flames. In Bulletin of the American Physical Society: 79th Annual Meeting of the Southeastern Section of the American Physical Society. 2012; Tallahassee, FL: paper k47.

Appendix

Appendix A: Calculation of Diatomic Spectra

Temperatures inferences in this study are made through comparisons of experimental and theoretical spectra. A complete and thorough explanation of how theoretical AlO spectra in this study are calculated is given in references (34) and (35). The theoretical spectra are calculated from tables of accurately calculated line strengths. The line strength, S_{ul}, of a transition from upper state, u, to lower state, l, is the sum of all degenerate diatomic states that produce the same spectral line and is related to the line intensity by

$$I_{ul} = \frac{64\pi^4 c\tilde{\nu}^4}{3(4\pi\epsilon_0)} S_{ul} N(n'v'J') \tag{A.1}$$

where $N(n'v'J')$ is the number of excited molecules, which is temperature dependent, and $\tilde{\nu}$ is the transition wave-number in vacuum. The diatomic state is defined by the quantum numbers n, v, J, and M for upper and lower states, where J and M represent their typical angular momentum quantum states, v represents the vibrational state, and n is an index used to represent all other relevant quantum numbers. The formal definition of the line strength is given as

$$S_{ul}(n'v'J'M', nvMJ) = \sum_{M'=-J'}^{J'} \sum_{M=-J}^{J} \left| \left\langle n'v'J'M' \left| \hat{T}^{(q)}_{M'-M} \right| nvMJ \right\rangle \right|^2 \tag{A.2}$$

where the primed values represent the upper transition state and the unprimed values represent the lower transition state. The operator $\hat{T}^{(q)}_{M'-M}$, is a spherical tensor operator that represents the qauntum mechanical electric dipole moment operator.

Diatomic spectra are calculated by determining the positions of all possible transitions, invoking selection rules to determine allowed and forbidden transitions, the Hönl-London factors, $S(J',J)$, are calculated, potential energy curves for allowed upper and lower transitions are determined, the Schrödinger equation is solved numerically to determine the Franck-Condon factors, $q(v',v)$, and the Hönl-London, Franck-Condon, and electronic transition strength are combined to form the total line strength. Rather than invoking the tedious process of using numerous selection rules for calculating diatomic spectra, only one selection rule is used in this study. An allowed tansition is one for which the line strength is nonvanishing and a forbidden transition is one for which the line strength vanishes. Numerically, the diatomic line strength is factored as described above and is calculated from

$$S_{ul}(n'v'J'M', nvMJ) = S_{electronic}(n'v', nv)q(v',v)S(J',J) \qquad \text{(A.3)}$$

where $S_{electronic}(n'v', nv)$ is the electronic transition strength. The Franck-Condon factors are found by numerically solving the Schrödinger equation and the Hönl-London factors are found from the diagnolized Hamiltonian for rotational and fine structure. Though both the Franck-Condon and Hönl-London factors may become appreciably small, it is the Hönl-London factor that determines if the line strength is analytically zero and thus determines allowed and forbidden transitions. Temperatures are inferred by considering the intensity that incident on a single detector pixel. At high number densities and high temperatures, with the time delays and gate widths employed in a typical LIBS experiment, thermal equilibrium of rotational and vibrational emissions are assumed.

Vita

David Surmick was born on February 6th, 1990 in Reading, PA. After graduating from Exeter Senior High school in 2008, David attended Lycoming College in Williamsport, PA where he majored in Astronomy and Physics. He graduated magna cum laude with departmental honors from Lycoming in 2012 with two undergraduate degrees, a Bachelor of Arts in Astronomy and a Bachelor of Science in Physics. As an undergraduate, David worked as a research volunteer while completing computational studies with gas burning flames. In August 2012 he entered the University of Tennessee Ph.D. physics program where he worked as a graduate research assistant at the Center for Laser Applications at the University of Tennessee Space Institute. While working there, David focused on projects that involved the characterization of aluminized flames and plasma. In August 2014 he earned his Master's of Science degree in physics from the University of Tennessee.